This accepted article to SciTech 2018 is made available by the authors in compliance with AIAA policy.
Please find the final, published version from ARC, DOI: 10.2514/6.2018-0532.

Scalability of Cyclic Control without Blade Pitch Actuators

James Paulos* and Mark Yim†
University of Pennsylvania, Philadelphia, PA 19104

Modulating the torque applied to a special flexible rotor can induce cyclic blade pitch changes which emulate the action of a conventional helicopter swashplate system. This attitude control technique has previously been applied to micro air vehicles as an alternative to multirotor distributed propeller arrays or helicopter servo and swashplate systems. This paper addresses the scalability of this method to both small future nano air vehicles and large manned aircraft. We develop scaling relationships which permit extrapolation of test data from one scale to another, and validate these results in test stand experiments using 10 cm diameter and 1 m diameter rotors. Modeling accuracy is improved by extending previous models to consider nonuniform blade mass distributions and employing noninvasive methods for the identification of inertial and electrical parameters of commercial off-the-shelf motor and electronic drive systems. Beyond isolated rotor testing we examine the impact of rotor size during vehicle design, gross trends with aircraft scale, and technology barriers to employing this technique in large scale manned flight.

I. Nomenclature

a	section lift curve slope
c	section chord length, m
c_{d_0}	section drag coefficient
c_β, c_ζ	equivalent flap and lag hinge damping
c_m, k_m	motor damping and stiffness coefficients
i, i_0	motor current and no-load current, A
I_β	flap inertia, kg m^2
I_h	hub inertia, kg m^2
K_e	motor emf constant, V/(rad/s) or N m/A
K_I, K_P	integral and proportional control gains
N_b	number of blades
R	blade tip radius, m
R_{ohm}	motor electrical resistance, ohms
u	additive modulation input
V	total motor terminal voltage, V
X_{I_h}	hub inertia ratio, $X_{I_h} = I_h/(N_b I_\beta)$
β	flap angle, rad
γ	Lock number, $\gamma = \rho a c R^4/I_\beta$
δ	skew lag-pitch hinge angle, rad
ζ	lag angle, rad
θ	blade pitch, rad
$\Delta\theta/\Delta\zeta$	geometric lag-pitch coupling coefficient
ρ	air density, kg/m^3
σ	rotor solidity, $\sigma = N_b c/(\pi R)$
$\phi_{3/4}$	downwash angle at 3/4 spanwise station, rad
ψ	hub orientation, rad
ω	hub speed perturbation, $\omega = \dot{\psi} - \Omega$, rad/s
Ω	hub speed average, rad/s

*Ph.D. Student, Mechanical Engineering and Applied Mechanics. Student Member AIAA.
†Professor, Mechanical Engineering and Applied Mechanics.

II. Introduction

Conventional helicopters practice cyclic blade pitch control in order to regulate their attitude during flight. For each revolution of the rotor blade, the blade pitch is actively varied in phase with the hub rotation. The resulting variations in aerodynamic angle of attack and lift result in both direct moments on the hub as well as coherent flapping motions which resolve as an apparent tilting of the tip path plane and effective thrust force. This complex response is conventionally initiated by a mechanical swashplate system which endeavors to kinematically prescribe the blade root pitch throughout each revolution of the rotor. This conceptual approach has remained essentially unchanged even through attempts to build ever larger transport helicopters and ever smaller micro air vehicles. However, at very small scales, the practical embodiment of the swashplate linkage system and ancillary actuators becomes fraught with difficulty. This has inspired a variety of alternative methods for attitude control including exotic swashplate systems, multi-rotor systems, gimballed motor thrust vectoring systems, and moving mass actuation.

A method for cyclic blade pitch control without the use of a mechanical swashplate or explicit blade pitch actuators has recently been demonstrated both in free flight micro air vehicles and test stand experiments at small scale. The premise is to endow one rotor blade with a positive lag-pitch coupling and the other rotor blade with a negative lag-pitch coupling. By modulating the drive motor torque through every rotation a lead-lag response can be excited which in turn drives a cyclic blade pitch variation. The resulting blade pitch changes, rotor flapping response, and aircraft flight response closely resemble the action of a conventional swashplate system. The natural question is whether this approach scales favorably, perhaps permitting the realization of extremely small future unmanned rotorcraft or new categories of large manned aircraft.

Section III describes the basic theory of operation for cyclic blade pitch control through torque modulation and reviews existing experimental results. Section IV details the construction of 10 cm diameter and 1 m diameter prototypes which have been designed to be dynamically similar. Section V reviews the fundamental equation of motion with new modifications to describe nonuniform blade mass distributions. A method for parameter identification in commercial off-the-shelf motor and drive systems is given in Section VI. The fundamental scaling trends inferred from the dynamic model are described in Section VII along with their impact on aircraft design and technology selection. Finally, test stand experiments in Section VIII verify these trends and the anticipated scale similarity of our 10 cm and 1 m prototypes.

III. Theory of Operation

The rotor system described here uses direct modulation of the driving hub torque to excite a desired dynamic response in specially designed flexible blades. In the two blade system, each blade is freely articulated to allow in-plane lead-lag and out-of-plane flapping motions about an offset hinge point. The rotor system is not symmetric. Rather, one blade has been designed with a positive lag-pitch coupling coefficient and the other blade has been designed by a negative lag-pitch coupling coefficient. The angle of inclination of a skewed lag-pitch hinge shown in Fig. 1 is used to control these coupling parameters.

As the applied motor torque is modulated, the two blades respond by leading and lagging cyclically in phase with the rotor rotation. From this synchronous motion, the opposite signs of their lag-pitch coupling result in 180° out of phase pitch variations. As one blade might be obtaining its maximum pitch across the nose of the aircraft simultaneously the other blade attains its minimum applied pitch across the tail. Since no auxiliary actuators or sensors have been added, both the amplitude and the phase of the cyclic blade pitch change must be controlled by the motor. The applied motor signal is the sum of two components. The first is the output of a conventional proportional-integral speed governor to maintain average head speed and thrust. The second component is a sinusoidal modulation whose amplitude determines the amplitude of cyclic pitch variation and whose phase is locked to the hub rotation in order to determine the direction of applied cyclic control.

Both test stand and free flight proof of concept demonstrations for this cyclic system have been shown previously [1]. Its implications for the design and power efficiency of new micro air vehicles has been discussed with further autonomous free flight experiments [2]. Most recently, a detailed dynamical model for the blade control system was validated against measured speed, lag, pitch, and flap variations during ground testing [3]. The prior work has all concerned similarly scaled micro air vehicle applications with a nominal diameter of approximately 30 cm. The purpose of this new study is to investigate the theoretical scalability and practical implementation of the system for very small and very large aircraft.

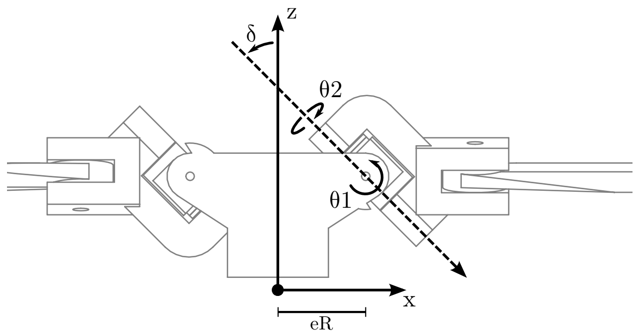

Fig. 1 Conventional flap and skewed lag-pitch axis [3].

IV. Prototype Construction

Two prototype rotors with diameters of 10 cm and 1 m were constructed. These prototypes were designed to be dynamically similar in the sense described in Section VII. The smaller 10 cm rotor depicted in Fig. 2 incorporates a 3.1 g AP03 brushless motor driven by a custom motor controller. The blade elements are 12 % thick flat plates with a chord of 5.6 mm constructed from pultruded carbon fiber. The hub is 3D printed from a photo cured resin, and the hinges are constructed from stainless steel pins in plain bores with PTFE thrust washers. Visible in the photograph of Fig. 2 are AprilTag fiducial markers [4] used for visual tracking of the blade motions during experiments. Rotor dimensions and properties are summarized in Table 1 and Table 2.

The larger 1 m rotor is driven by a 1280 g T-Motor U13 brushless motor with a custom logic controller driving the power stage of a commercial off-the-shelf hobby grade electronic speed controller. The blade elements are 10 % thick flat plates with rounded edges with a chord length of 56 mm machined from acetal plastic. The hub and blade grips are machined from aluminum and use sintered bronze flanged bushings to support 0.25 in diameter stainless steel hinge axles. The photograph of Fig. 3 shows the power stage used to drive the motor along with the 1 m prototype. The AprilTag fiducials used during experiments are shown in Fig. 4 along with an inertial flybar added to establish dynamic similarity between the large and small rotors by accounting for the inherent difference in the motor inertias.

Table 1 Rotor assembly properties.

parameter	symbol	small	large
tip radius	R	5 cm	50 cm
blade chord	c	5.9 mm	59 mm
blade mass	m	0.39 g	362 g
flap inertia	I_β	1.8×10^{-7} kg m^2	1.7×10^{-2} kg m^2
total hub inertia	-	5.2×10^{-8} kg m^2	5.1×10^{-3} kg m^2

Table 2 Motor properties.

parameter	symbol	small	large
emf constant	K_e	0.0025 V/(rad/s)	0.11 V/(rad/s)
resistance	R_{ohm}	1.4 ohms	0.24 ohms
motor rotational inertia	-	3.9×10^{-8} kg m^2	1.0×10^{-3} kg m^2

Table 3 Nondimensional Parameters.

parameter	symbol	small	large
hinge eccentricity	e	0.09	0.09
blade radius of gyration	l	0.426	0.435
blade radius of oscillation	k	0.607	0.624
rotor solidity	σ	0.0746	0.0746
collective pitch	θ_0	9°	8°
lag-pitch coupling	$\frac{\Delta\theta}{\Delta\zeta}$	1	1
hub inertia ratio	X_{I_h}	0.147	0.148
lift curve slope	a	6.28	6.28
drag coefficient	c_{d_0}	0.06	0.06
Lock number	γ	1.56	1.61
structural lag damping	c_ζ	0.0751	0.0899
structural flap damping	c_β	0.0381	0.0385
drive induced stiffness	$\frac{k_m}{I_\beta \Omega^2}$	9×10^{-5}	9×10^{-5}
drive induced damping	$\frac{c_m}{I_\beta \Omega}$	9×10^{-2}	9×10^{-2}

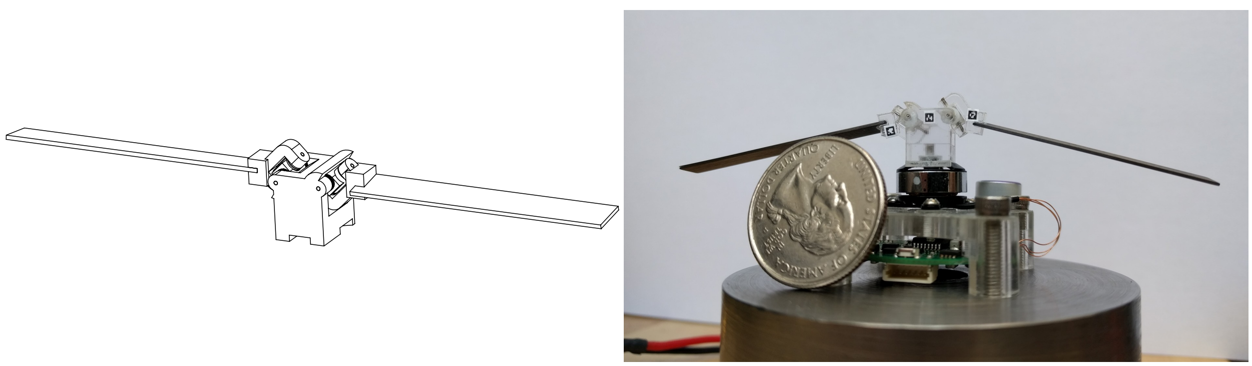

Fig. 2 10 cm diameter rotor.

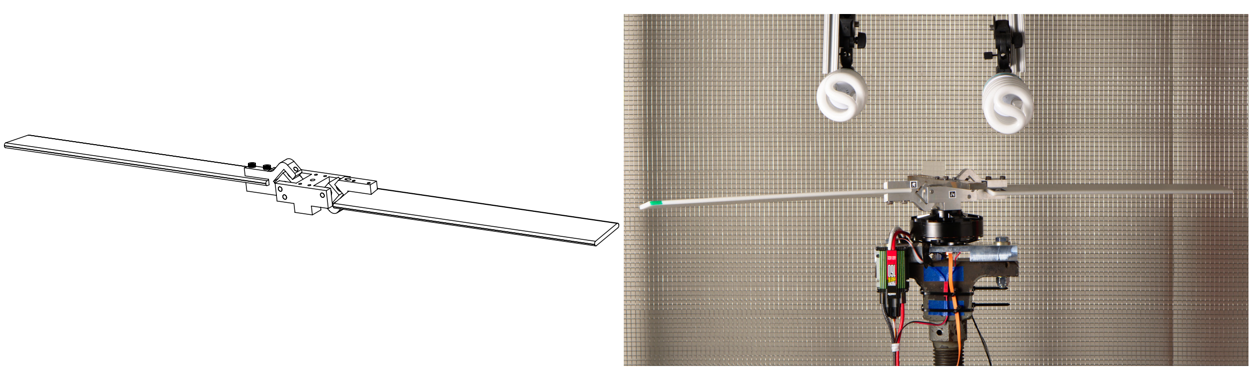

Fig. 3 1 m diameter rotor.

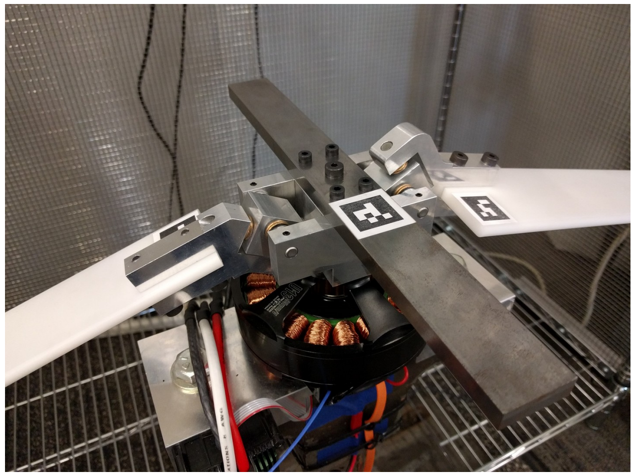

Fig. 4 Hub inertia augmented with flybar to obtain dynamic similarity.

V. Equations of Motion

The dynamical model for the rotor system including motor dynamics and a variable hub speed has been derived in previous work [3] and is presented below, followed by a brief description of the main elements. For small blade deflections, the motions of the true kinematic structure shown in Fig. 1 can be modeled in terms of the canonical flap and lag coordinates shown in Fig. 5 if an additional lag-pitch coupling $\Delta\theta/\Delta\zeta = \tan(\delta)$ is imposed. Equation 1 gives the governing equations for a single blade in rotating coordinates in terms of the state vector $\boldsymbol{x}$ consisting of virtual hub displacement $\tilde{\psi}$, lag angle ζ, and flap angle β. The model is linearized about a mean operating speed of Ω where trim lag angle and flap angle biases ζ_0 and β_0 have been obtained. Prime derivatives denote derivatives with respect to the rotating azimuthal frame such that coordinate rates are normalized by the hub speed Ω and an angular velocity of one indicates a once-per-revolution oscillation. The single input u is the nondimensionalized modulation of the applied motor drive voltage.

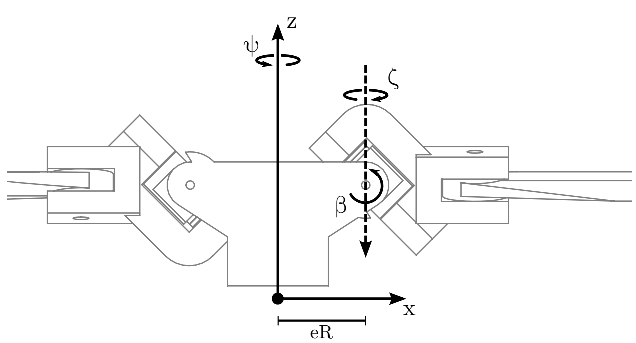

Fig. 5 Virtual hub, lag, and flap axes for modeling [3].

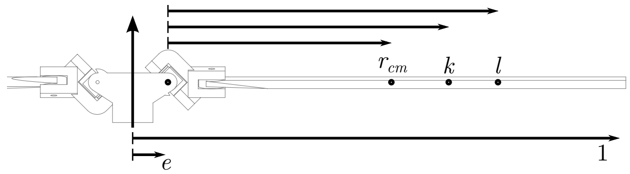

Fig. 6 Inertial parameterization in terms of radius of gyration k and radius of oscillation l.

$$
\begin{aligned}
&\begin{bmatrix} 1 + X_{I_h} + 2\frac{e}{l} + \frac{e^2}{k^2} & -1 - \frac{e}{l} & 0 \\ -1 - \frac{e}{l} & 1 & 0 \\ 0 & 0 & 1 \end{bmatrix} \boldsymbol{x}'' + \left(\begin{bmatrix} \frac{c_m}{\Omega I_\beta}/N_b & -2\frac{e}{l}\zeta_0 & -2(1+\frac{e}{l})\beta_0 \\ 2\frac{e}{l}\zeta_0 & c_\zeta & 2\beta_0 \\ 2(1+\frac{e}{l})\beta_0 & -2\beta_0 & c_\beta \end{bmatrix} \right. \\
&\left. + \frac{1}{8}\gamma \begin{bmatrix} (2\frac{c_{d_0}}{a}+\theta_0\phi_{3/4}) & -(2\frac{c_{d_0}}{a}+\theta_0\phi_{3/4})(1-\frac{4}{3}e) & (\theta_0-2\phi_{3/4})(1-\frac{4}{3}e) \\ -(2\frac{c_{d_0}}{a}+\theta_0\phi_{3/4})(1-\frac{4}{3}e) & (2\frac{c_{d_0}}{a}+\theta_0\phi_{3/4})(1-\frac{8}{3}e+2e^2) & -(\theta_0-2\phi_{3/4})(1-\frac{8}{3}e+2e^2) \\ -(2\theta_0-(1+\frac{c_{d_0}}{a})\phi_{3/4})(1-\frac{4}{3}e) & (2\theta_0-(1+\frac{c_{d_0}}{a})\phi_{3/4})(1-\frac{8}{3}e+2e^2) & (1+\frac{c_{d_0}}{a})(1-\frac{8}{3}e+2e^2) \end{bmatrix} \right) \boldsymbol{x}' \\
&+ \left(\begin{bmatrix} \frac{k_m}{\Omega^2 I_\beta}/N_b & 0 & 0 \\ 0 & \frac{e}{l} & 0 \\ 0 & 0 & 1+\frac{e}{l} \end{bmatrix} + \frac{1}{8}\gamma \begin{bmatrix} 0 & \phi_{3/4}\frac{\Delta\theta}{\Delta\zeta} & 0 \\ 0 & -\phi_{3/4}(1-\frac{4}{3}e)\frac{\Delta\theta}{\Delta\zeta} & 0 \\ 0 & -(1-\frac{4}{3}e)\frac{\Delta\theta}{\Delta\zeta} & 0 \end{bmatrix} \right) \boldsymbol{x} = \begin{bmatrix} \frac{\gamma}{a\sigma} \\ 0 \\ 0 \end{bmatrix} u
\end{aligned} \tag{1}
$$

The nondimensional parameters which appear in the inertia tensor and Coriolis matrix include the hinge location eccentricity e, the hub inertia ratio X_{I_h}, the blade radius of gyration k, and the blade radius of oscillation l. The nondimensional parameterization defined in Eq. 2 and graphically illustrated in Fig. 6 provides a description of blades with arbitrary mass distributions and inertial properties which might otherwise be described in terms of their dimensional flap inertia I_β, blade mass m, tip radius R, and fractional location of the center of mass r_{cm}. The specialized forms of the inertia tensor and Coriolis matrix reported previously [3] for a uniform blade mass distribution can be obtained from the general result in Eq. 1 by substituting the specialized values of the radius of gyration $k^2 = (1-e)^2/3$ and radius of oscillation $l = 2(1-e)/3$. Practical fabrication of the tiny 5 cm blades used in this work results in the mass being biased towards the root where the hinge attachment sits, so modeling this mass distribution is necessary for accurate predictions of the inertial dynamic response.

$$
\begin{aligned}
l &= \frac{I_\beta}{r_{cm} m R^2} \\
k^2 &= \frac{I_\beta}{m R^2}
\end{aligned} \tag{2}
$$

Aerodynamic forces are modeled using a representative lift curve slope a, drag coefficient c_{d_0}, collective blade pitch θ_0, and downwash angle $\phi_{3/4}$ [3]. The lag-pitch coupling enters as the constant $\Delta\theta/\Delta\zeta$. Standard definitions for the Lock number γ and rotor solidity σ have been used.

Hinge friction has been modeled using energy equivalent damping coefficients c_ζ and c_β which have been defined in previous work as a function of hinge design parameters. Finally the combined effects of the motor dynamics and the speed governor controller are described by gain constants k_m and c_m. These coefficients depend on both physical motor parameters such as the emf constant K_e and electrical resistant R_{ohm} and software defined proportional and integral gains of the speed governor, K_P and K_I, as shown in Eq. 3 [3]. The scalar input u to the system in Eq. 1 represents the additive voltage modulation $\tilde{V}$ applied to the motor to induce a cyclic response about trim. It is defined in Eq. 4 nondimensionalized in a similar form as the conventional torque coefficient for rotors.

$$
c_m = (K_P + K_e)\frac{K_e}{R_{ohm}} \qquad k_m = K_I \frac{K_e}{R_{ohm}} \tag{3}
$$

$$u = \frac{1}{\rho \pi R^5 \Omega^2} \frac{K_e}{R_{ohm}} \tilde{V} \tag{4}$$

VI. Motor Parameter Estimation

An accurate model for the combined electromagnetic motor and associated drive electronics is needed in order to correctly describe the dynamic blade response to modulation of the applied motor voltage. Commercial off-the-shelf motors for MAV applications are typically not fully specified by the manufacturer and are susceptible to manufacturing variations from device to device. Furthermore, commercial motor controller electronics typically employ proprietary designs and do not specify electrical properties such as their output impedance. This section describes a noninvasive system identification method appropriate for dealing with uncertain motor and drive properties which requires no external torque sensing.

We assume the basic DC motor model given by Eq. 5. The motor velocity ω accelerates subject to the instantaneous motor torque τ and motor inertia I. The torque τ is a function of the electrical current i, constant no load current i_0, and motor electromotive force constant K_e. The current is driven by an applied terminal voltage V and subject to speed ω, constant K_e, and effective series resistance R_{ohm}.

$$\begin{aligned} \dot{\omega} &= \frac{1}{I}\tau \\ \tau &= K_e(i - i_0) \\ i &= \frac{1}{R_{ohm}}(V - K_e\omega) \end{aligned} \tag{5}$$

This system is linearized about an operating speed Ω to obtain Eq. 6. In Eq. 6 and through the remainder of this section ω and τ implicitly refer to variations from the steady state.

$$\begin{aligned} \dot{\omega} &= \frac{1}{I}\tau \\ \tau &= \frac{K_e}{R_{ohm}}(V - K_e\omega) \end{aligned} \tag{6}$$

The system identification problem reduces to identifying three parameters: the motor constant K_e, effective resistance R_{ohm}, and rotational inertia I.

Motor parameters K_e, R_{ohm}, and I can be determined using only speed measurements by observing the frequency response to applied voltage with two or more different known added inertial loads I_j. Since the dynamic range of torque transducers is limited, this method may be more convenient for very small and very large motors such as those depicted in Fig. 2 and 3. It can also be accomplished without any external instrumentation, requiring only the ability to manufacture disks with a known inertia.

The applied voltage to speed variation transfer function for the motor inertia I with an added inertia I_j is shown in Eq. 7. The added inertia will tend to increase the time constant $(I + I_j)R_{ohm}/K_e^2$ as shown in the Bode plots of Fig. 7.

$$\frac{\omega}{V} = \frac{1}{K_e} \cdot \frac{1}{\frac{(I+I_j)R_{ohm}}{K_e^2}s + 1} \tag{7}$$

Fitted values for the two transfer function coefficients in Eq. 7 can be used to calculate the two parameter groups K_e and the product $(I + I_j)R_{ohm}$. By repeating the experiment $N \geq 2$ times with known values of I_j we can find the least squares solution for I and R_{ohm} by solving N equations in two unknowns. This regression is illustrated graphically in Fig. 7, where the slope gives the resistance and the y-intercept gives the inertia-resistance product for the bare motor with no added inertia from flywheels.

As the motor control designer we can apply some additional insight into the filter dynamics of the speed measurement. For these experiments speed measurements from the encoder are oversampled at high rate and passed to a first order low pass filter with corner frequency of $f_c = 1000\,\text{Hz}$. The expected transfer function from true speed ω to observed speed $\hat{\omega}$ is given by Eq. 8. In practice only the residual frequency response is fitted to the motor model, reducing the modeling discrepancy.

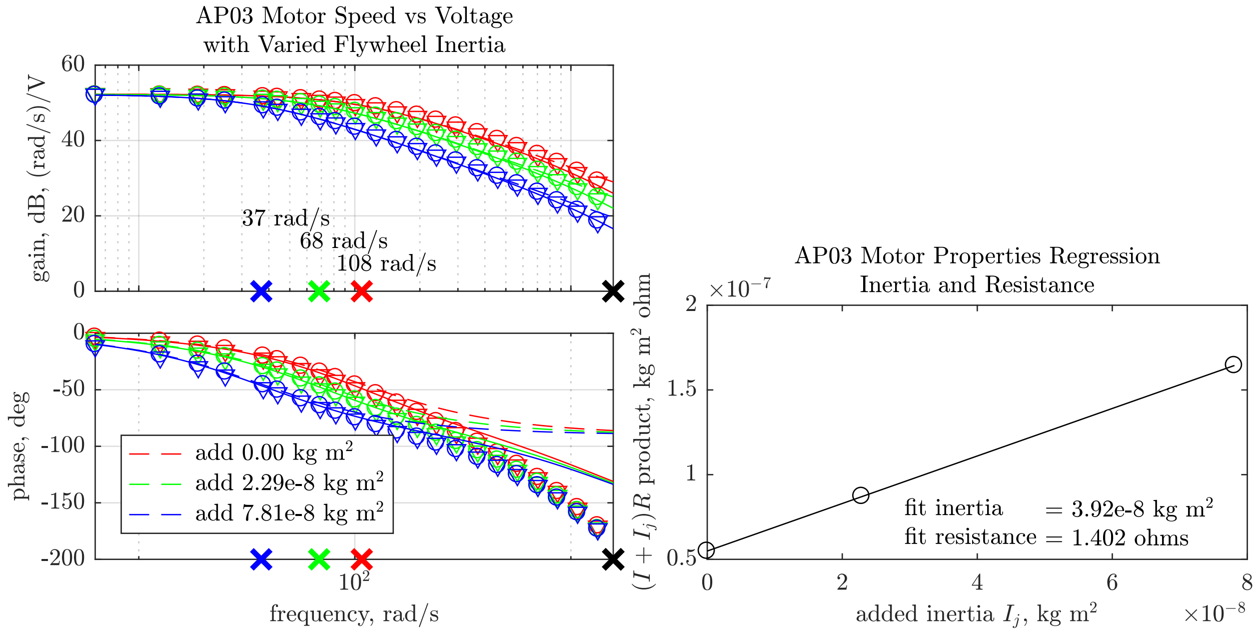

Fig. 7 Small motor properties by regression from frequency domain data.

$$\frac{\hat{\omega}}{\omega} = \frac{1}{\frac{1}{2\pi f_c}s + 1} \tag{8}$$

Figures 7 and 8 show the total modeled transfer function fit in solid lines and the associated motor model in dashed lines to depict the corrective impact of this measurement model, most apparent at higher frequencies. The additional phase loss observed at high frequency may be due to unmodeled time delays associated with the digital controller or low pass dynamics of the power electronics. The identified parameters from these bare motor tests are used to generate the model predictions for the full rotor system validated during cyclic experiments.

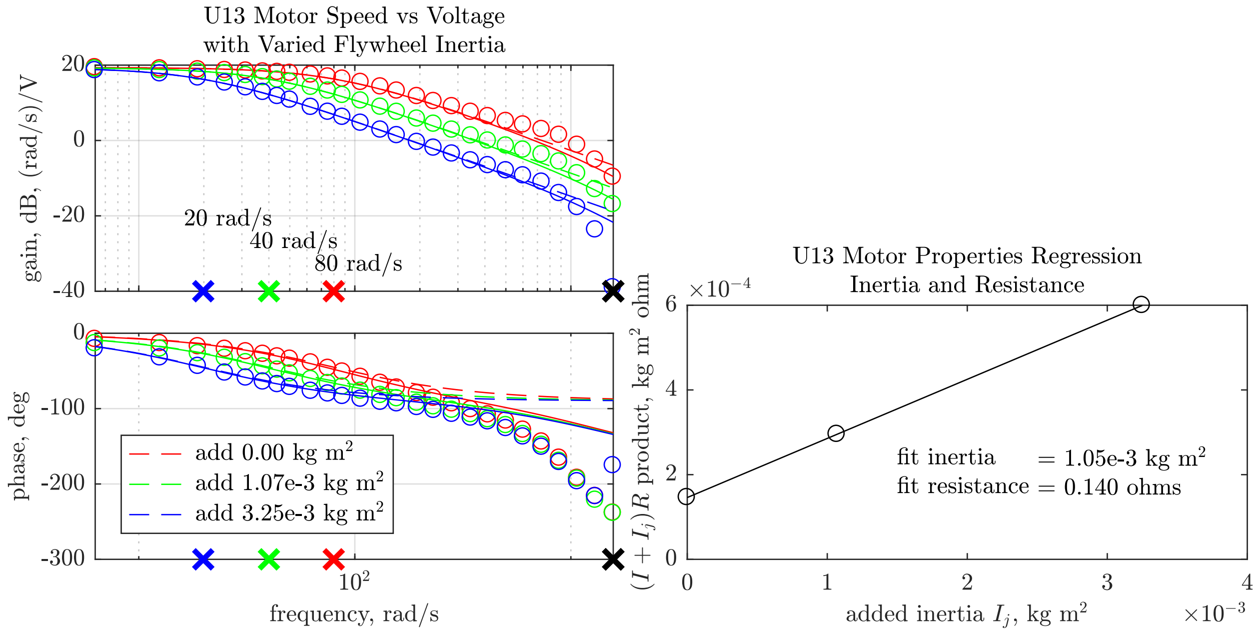

Fig. 8 Large motor properties by regression from frequency domain data.

VII. Scaling

Mechanical swashplate control systems have been successfully deployed in vehicles as small as the 16 g Black Hornet and as large as a 56,000 kg loaded Mi-26 transport helicopter. A natural question arises as to whether the dynamic cyclic approach has similar scalability. There are several interrelated facets of the scale problem spanning rotor design and vehicle integration. How do we design dynamically similar rotor experiments, and how do we extrapolate isolated rotor test results across differences in scale and operating speed? In the context of aircraft design, what are the consequences of varying rotor size and speed for a fixed aircraft? Finally, what are the general scaling characteristics when the dynamic cyclic system is applied to conceptual aircraft across vastly different scales?

Given the historical importance of scale model testing to the design and development process in aerospace, the subject has received a great deal of attention. The proper application of scaling analysis depends on the purpose of the study. This is why we find Mach number and Reynolds number similarity emphasized when interpreting isolated rotor tests [5, 6], but Froude number is of great importance to vehicle flying qualities [7–10], and power considerations can give direct insight into vehicle design [11, 12]. For this reason the appropriate framework of assumptions shifts while consideration of each of the three motivating questions in turn.

A. Rotor Scale Testing

Isometric scaling is an seemingly obvious requirement for discussing the scaling behavior of an isolated rotor; we frequently wish to consider a family of rotors which have similar geometry but differ in absolute size. A more significant property is to have strict scaling in the dynamic behavior. A set of dynamically similar experiments at different scales can all be described by one single nondimensional equation of motion. The design of such experiments must simultaneously consider both the model construction and also the operating condition. Dynamic similarity is required to conduct meaningful scale model testing. It allows us to extrapolate motions and forces from one isolated test stand experiment or numeric simulation to a continuous family of similar rotors both large and small.

1. Prescriptive Requirements for Dynamic Similarity

This section develops specific prescriptive requirements for dynamic similarity between rotors which may be used to guide the design of experiments, and it comments on the consequent scaling of physical quantities in the blade response. A treatment of aeroelastic helicopter blades by Hunt based on dimensional analysis identifies nine relevant independent variables governing the rotor involving three physical units (mass, length, and time). Therefore, the Buckingham Pi

Table 4 Characteristic scales for nondimensionalization.

quantity	normalized by
inertia	I_β
length	R
angular rate	Ω

Table 5 Nondimensional parameter groups.

variables	quality
e, l, k, θ_0, σ, N_b, $\frac{\Delta\theta}{\Delta\zeta}$	geometry
X_{I_h}	ratio of inertias
a, c_{d_0}	aerodynamics
γ	ratio of aerodynamic to inertial forces
c_ζ, c_β	structural damping
$\frac{k_m}{I_\beta \Omega^2}$, $\frac{c_m}{I_\beta \Omega}$	motor and controller

Theorem permits the selection of six governing nondimensional parameters. Conventionally, these are the Reynolds number, Mach number, Froude number, advance ratio, ratio of aerodynamic to inertial forces (Lock number), and ratio of aerodynamic to elastic forces [5]. It is in fact generally infeasible to maintain similarity across all six parameters, and this particular list is neither unique, necessary, nor exhaustive for all purposes.

We can obtain specific criterion for achieving similarity in dynamic cyclic rotors directly from the governing equations of motion. In developing those equations we selected dimensional normalizing factors for inertia, length, and angular rate listed in Table 4.

This basis spans the salient fundamental units of mass, length, and time for the problem if we postpone discussion of the electric motor's operation. These three parameters disappear from the equation of motion after normalization, leaving 15 independent parameters to consider governing Eq. 1. For strict dynamic scaling the values of these 15 nondimensional parameters or parameter groups must be preserved. Table 5 groups these parameters by their associated design considerations required in order to construct properly scaled experiments.

The numerous geometric parameters are preserved simply by maintaining geometric similarity between rotors.

Combining isometric scaling with constant mass density will also preserve the inertia ratio X_{I_h} between the hub inertia and the blade flap inertia. In practical applications, motors are selected based on the application's torque demands and not something as arbitrary as the motor's physical size. Consequently, maintaining the inertia ratio for dynamically similar experiments requires either contrived physical motor selection or augmenting the hub with inertial masses as shown in Fig. 4.

The impact of aerodynamics have been summarized by a simple linear aerodynamics model incorporating a lift curve slope a and drag coefficient c_{d_0}. In addition to the airfoil geometry, these parameters are in general dependent on the local Reynolds number, *Re*, describing the ratio of inertial forces to viscous forces in the flow and the Mach number, *Ma*, describing the ratio of the flow speed to the speed of sound in the fluid medium. For testing in air at atmospheric pressure it is not possible to simultaneously preserve both Reynolds number and Mach number [5]. However, the lift curve slope is relatively insensitive to small changes in Reynolds number except at very low values, and variations in the drag coefficient are of secondary importance to the system dynamics. If desired, equal Mach numbers are easily obtained by operating at equal tip speeds, but these rotors operate far below their critical Mach number and so variations due to Mach number are small. Consequently, at this level of modeling detail, it is fairly reasonable to consider a and c_{d_0} to be independent constant values associated with the airfoil geometry.

The ratio of aerodynamic to inertial forces on the blade appears in the equations of motion as the Lock number, γ. If geometric similarity, constant mass density, and aerodynamic similarity have been preserved then the Lock number too will be preserved.

Structural damping effects in this model are lumped parameters associated with the hinges. The energy equivalent

Table 6 Dimensional basis and isometric scaling result for model quantities.

quantity	normalized by	isometric scaling
length	R	R
mass	$I_\beta R^{-2}$	R^3
inertia	I_β	R^5
time	Ω^{-1}	Ω^{-1}
angular rate	Ω	Ω
force	$I_\beta \Omega^2 R^{-1}$	$R^4\Omega^2$
torque	$I_\beta \Omega^2$	$R^5\Omega^2$

nondimensional damping coefficients c_ζ and c_β are shown in [3] to remain constant under isometric scaling assuming constant material friction coefficients.

Finally, the virtual damping and stiffness afforded by the motor and motor controller described by nondimensional parameters k_m and c_m must be held constant for proper dynamic scaling. The definition of these parameters in Eq. 3 shows them to be functions of both the motor's physical properties (electromotive force constant K_e and resistance R_{ohm}) and the freely chosen software control gains (proportional gain K_P and integral gain K_I). As a result, the critical parameters k_m and c_m can be maintained by applying the correct software gains.

The above nondimensional parameters differ slightly from those identified by Hunt [5]. Since the present analysis considers the near hover condition, the advance ratio is always zero. We additionally do not model gravitational forces on the blade, so the Froude number is irrelevant. If the weight of the blades were to significantly change the coning angle this might be questioned, something possible at artificially low thrust levels. Finally, this model does not incorporate structural elastic effects since the blades are rigid and the hinges have no intrinsic spring stiffness. On the other hand, we explicitly model structural damping through the hinge losses, an effect that is often ignored.

2. Extrapolation of Experimental Results across Scale and Speed

Having specified criterion for dynamic similarity, we can observe trends in the response of similar rotors at differing size or operated at different speeds. Table 6 associates dimensional quantities such as length or torque with the dimensional basis used to normalize them in the equation of motion, a function of length R, angular rate Ω, and flap inertia I_β. The inertia scales as R^5 under isometric scaling with constant material density, and so for similar rotors these quantities are shown to grow in proportion to products of powers of the rotor radius R and operating speed Ω.

Table 6 shows that torques grow with the square of operating speed and to the fifth power of radius. In particular the aerodynamic drag torque, and therefore the mean motor torque, grow as $R^5\Omega^2$. This is the conventional result which motivates defining torque and power coefficients for propellers. This result extends to the dynamic rotor response to torque modulation. The amplitude of the motor torque modulation must grow commensurate with the motor drag torque as $R^5\Omega^2$ in order to obtain a similar response in terms of pitch variation or flap angle. Of course, the ultimate useful pitching torque obtained will also rapidly grow as $R^5\Omega^2$. As a result, larger or faster rotors obtain larger useful pitching moments at the expense of proportionally larger drive torques.

The time scale of the transient dynamic response is also of interest; it limits how rapidly the amplitude or azimuthal phase of the rotor response can be varied to pitch or roll the aircraft. Within the linear and time invariant model framework, a metric for this response time is given by calculating the inverse of the real part of the system poles. For similar rotors the transient decay time constant increases proportional to $1/\Omega$, so faster spinning rotors are capable of affecting more rapid changes in roll or pitch commands, independent of size.

The experimental results shown in Section VIII both confirm and take advantage of these scaling trends. Experiments across an order of magnitude in scale and operating speed obtain similar hub speed responses scaled by $1/\Omega$ and similar blade deflection angles when the applied modulation u is normalized by $R^5\Omega^2$ as defined in Eq. 4.

B. Impact of Rotor Size

Rotor sizing is an important part of aircraft design. This section will no longer suppose the kind of arbitrary changes to rotor size or operating speed possible in synthetic test stand experiments. Instead we will consider the impact of

Table 7 Scaling at constant thrust.

quantity	scaling
length	R
mass	R^3
inertia	R^5
time	R^2
angular rate	R^{-2}
force	1
torque	R

moderate changes in rotor size for a given aircraft with a fixed hover thrust requirement. From Table 6 in the previous section we saw that the thrust force is proportional to $R^4\Omega^2$, so to maintain a constant thrust with similar rotors the speed must change in proportion to the inverse square of radius, holding $R^2\Omega$ constant. We can recast Table 6 to show how the rotor dynamic quantities scale under this new constraint in Table 7.

As before, the pertinent torques all scale together for dynamically similar operation. These include the motor's modulation amplitude torque, the useful pitching reaction torque, and the steady drag torque. In particular, the ratio of the motor's modulated torque amplitude to the resulting useful pitching reaction torque remains constant for different sized rotors when operated at the same thrust level and cyclic pitch variation. At the same time, in absolute terms, these torques increase with R.

Given two similar rotors operating at the same thrust level and same cyclic pitch variation, we should expect that the larger rotor generates larger pitching moments in proportion to R. Within a fully linear model framework, this implies that the larger rotor could be operated with a cyclic pitch variation of $1/R$ that of the small rotor in order to obtain the same same pitching moment effect. This requires an assumption of linearity to justify and is not a generic scale argument since the two hypothetical rotors are being driven at different cyclic amplitudes. The required driving modulated torque amplitude then remains constant as $1/R \times R = 1$, independent of size. Changing rotor size while operating at fixed thrust does not change the modulated torque amplitude required to obtain a particular vehicle pitching moment.

Since the drag torque of the larger rotor grows as R while the torque modulation requirement remains constant, the torque modulation described as a percentage of the steady operating torque falls. As a consequence, the drive system for the larger rotor does not need to be oversized by as large a safety factor to tolerate pulsing operation.

The transient response time of the rotors slow as R^2, consistent with our understanding that operating a bigger rotor at the same thrust level implies a slower operating speed. The ability to manipulate the blade pitch through an azimuthal rotation of the hub is unaffected – but the rotor spins more slowly and so the effective bandwidth of vehicle control should be expected to fall off in a similar way to the trend in conventional helicopters with kinematic swashplate systems.

The trends developed in this section are useful for contemplating small changes to the nominal rotor size for a fixed aircraft. In practice, the weight of the rotor must factor into the rotor thrust requirement, so contemplating massive rotors on vehicles with a tiny thrust requirement is unreasonable. Likewise, it is not practical to speak of tiny rotors whose size approach zero and require impossibly large speeds. More fundamentally, requiring a fixed thrust from radically different size rotors preserves the Reynolds number ($Re \propto \Omega R^2 \propto 1$) but entails massive variation in the Mach number ($Ma \propto \Omega R \propto 1/R$) and the rotor Froude number ($Fr \propto \Omega^2 R \propto 1/R^3$) affecting both aerodynamic forces and material stresses. As a result, the assumption that dynamic similarity can be maintained for the rotor at all is highly questionable.

C. Impact of Vehicle Size

Finally we come to the question of rotor control technology selection in new aircraft. Is dynamic cyclic more or less suitable for very small or very large aircraft? In the previous section it was shown that holding thrust constant and increasing the rotor size reduces the proportional motor torque modulation requirements but also slows the response time. To look at trends across vehicle sizes, we need a presumptive rule to correlate vehicle mass (or thrust requirement) to rotor size and speed.

Figure 9 correlates helicopter mass and rotor diameter for a variety of electric and combustion engine aircraft across more than six orders of magnitude in weight. The manned aircraft data primarily comes from a survey by Lorenz [11]

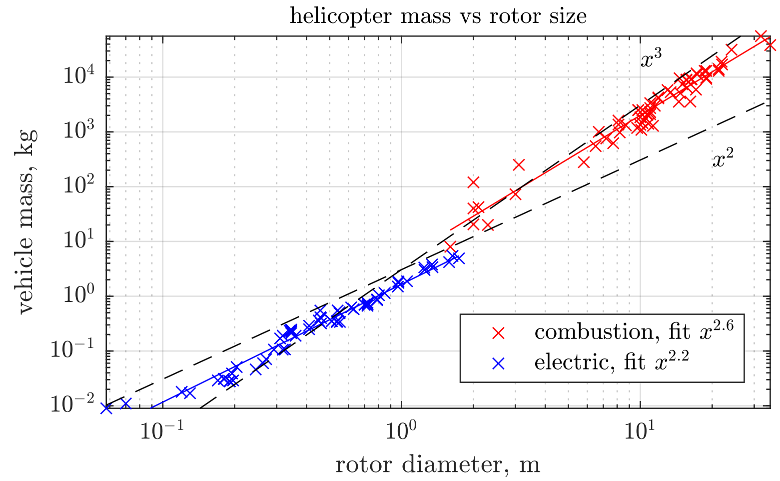

Fig. 9 Production helicopter mass vs rotor diameter.

Table 8 Froude scaling for isometric vehicle and rotor growth.

quantity	isometric scaling
length	R
mass	R^3
inertia	R^5
time	$R^{1/2}$
angular rate	$R^{-1/2}$
force	R^3
torque	R^4

and the unmanned aircraft information is primarily sourced from marketing materials. The logarithmic plot displays quadratic and cubic growth trends for comparison. Generally speaking, helicopter mass grows with rotor diameter slower than isometric scaling would predict, $W \propto R^3$. Larger helicopters have proportionality larger rotors than isometric scaling would suggest. On the other hand, weight grows faster with rotor size than constant disc loading would predict, $W \propto R^2$. As a consequence, larger helicopters must operate at a higher ideal specific power than smaller helicopters on a watts-per-kilogram basis [11]. Separate best fit trends are shown for the exponent of growth for surveyed combustion helicopters ($R^{2.6}$) and electric helicopters ($R^{2.2}$).

Some caution must be exercised in interpreting this plot, as these aircraft represent a wide range in technologies and have been optimized for disparate missions. The data includes heavy transport helicopters at their maximum laden capacity right alongside unmanned electric sport aircraft. Perhaps this explains the apparent difference in weight growth exponent between the two vehicle classes. Electric sport helicopters all rely on the same technologies of lithium polymer batteries and electromagnetic motors and are designed to optimize flight performance with no payload, so their design may be constrained closer to a constant specific power curve by their constitutive technologies.

The majority of scaling analyses assume isometric scaling of the gross vehicle and rotor size together, with the result that the vehicle mass grows as R^3. Table Table 6 shows that the rotor's thrust force grows as $R^4\Omega^2$, so similar rotors will need to be operated such that $R\Omega^2$ remains constant in order to maintain the balance of aerodynamic to gravitational forces for the vehicle. This is Froude scaling applied to both the rotor and the vehicle dynamics. The consequences of this in terms of the magnitude of forces, torques, and time scales are shown in Table 8.

These results are identical to the analysis of Froude scaling as a model for conventional helicopters given in [8], suggesting that the principle scaling factors relevant to conventional helicopters carry over to the dynamic cyclic system. In particular, larger helicopters are less agile as their rotor response times increase with $R^{1/2}$ and their body angular accelerations due to control torques decrease as $1/R$. Assuming these generic trends are satisfactory, the ratio of modulated torque to rotor drag torque and therefore the motor sizing safety factor needed to exercise dynamic cyclic remains constant. In the limited sense of the fundamental blade dynamics, then, absolute scale does not significantly impact the feasibility of cyclic blade pitch control through hub torque modulation.

D. Practical Limitations for Manned Helicopters

While the fundamental physics involved in dynamic cyclic control scales similarly to conventional swashplate cyclic systems, dynamic cyclic presents unique challenges for large scale or manned aircraft. The principle technological difficulty is in pulsing the drive torque applied to the hub at the rotor frequency. This is easy to do with electromagnetic drive motors whose torque response time is significantly faster than the rotor's rotational period. However, small manned helicopters typically employ reciprocating combustion engines and large, high performance helicopters rely on turboshaft engines [13]. A representative time constant describing the torque response to a step increase in fuel flow for the T700 turboshaft engine is 0.6 s and for a step decrease in fuel flow 0.8 s [14]. As a result, torque modulation at a characteristic rotor frequency near 300 RPM (5 Hz) is impractical [15]. As a result, either an alternative propulsion method such as electronic motors or some auxiliary modulation actuator would be required. All-electric helicopters remain an open area of research bringing their own difficulties, and the introduction of additional actuators reintroduces some of the complexity one hopes to avoid by removing the swashplate system.

Safety and redundancy challenges associated with implementing dynamic cyclic are perhaps the more fundamental barrier to using laboratory scale MAV as a literal blueprint for manned aircraft. Conventional manned helicopters incorporate collective blade pitch control in addition to cyclic blade pitch control, which allows them to exploit autorotation for a controlled descent in the case of engine failure. Since the present system does not incorporate collective blade pitch control it can not autorotate safely in this manner. More importantly, a conventional helicopter's attitude control is approximately decoupled from the thrust power plant, and this enables the aircraft to maneuver even after suffering an engine loss. In contrast, if a single electric motor is the sole actuator onboard, its loss leads not just to rapid descent but to complete loss of attitude control.

VIII. Cyclic Experiments

A set of test stand experiments were undertaken to establish the validity of the dynamic model for both a 10 cm and 1 m diameter rotor as well as verify the expected scaling trends developed in Section VII. Similar to the methodology in [3], the rotors were each evaluated at three different trim speeds. At each speed an additive, sinusoidal voltage modulation was applied as a function of the azimuthal hub angle, resulting in cyclic variations in motor torque, hub speed, blade lag, pitch, and flap. The hub speed was determined by a rotary encoder, lag angles were determined from overhead high speed video using fiducial markers, and flap angles were determined by stroboscopic photography from the side. The speed and blade motions are summarized by an amplitude and phase of response at a range of applied drive amplitudes.

Figures 10 and 11 depict the hub speed variation response to changes in the normalized drive voltage amplitude u at several different test speeds from approximately 300 RPM to 9000 RPM. Since these rotors have been designed and operated to be dynamically similar the model prediction curves are very similar for both rotors when plotted nondimensionally. The first set of plots show the amplitude of the hub speed response to a range of input voltage amplitudes. There is a knee in the response at low amplitude for both rotors where static friction is broken, and then a linear growth in the response closely adhering to the model prediction. At high drive amplitudes the response flattens out, which correlates with the blade audibly hitting hitting hard kinematic stops during the experiments. The second plot shows for the same experiments the phase of the hub speed response relative to the phase of the input sinusoid. There is again a strong nonlinear distortion at low amplitude due to friction and then convergence towards a fixed value at higher amplitudes. At high amplitudes the measured phase response adheres to the model within approximately 10°. The degree to which the data taken at very different speeds and on very different scales overlays on the nondimensional plot verifies the utility of the nondimensional dynamic model.

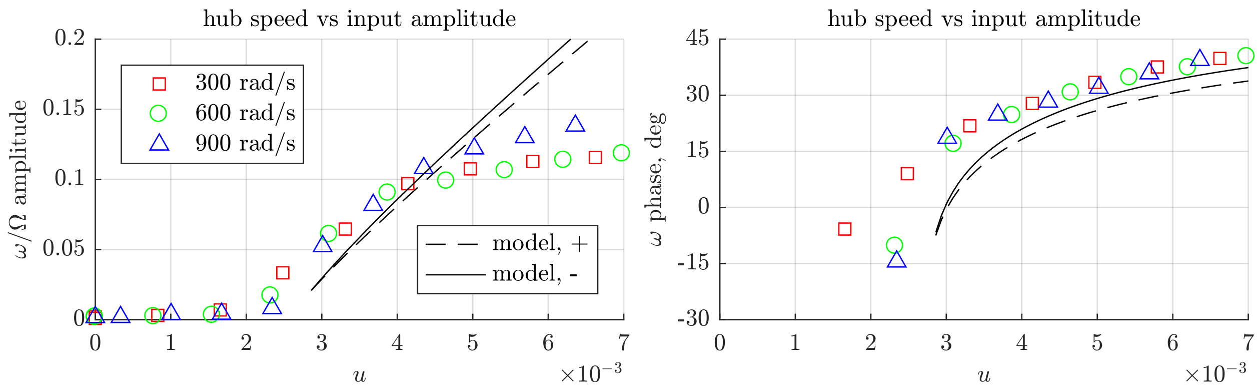

Fig. 10 Hub speed response in small rotor.

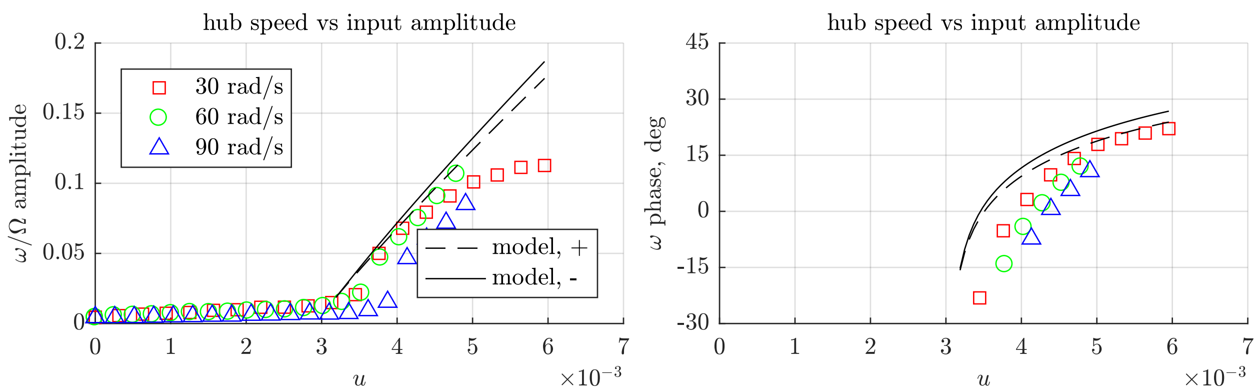

Fig. 11 Hub speed response in large rotor.

The blade lag response may be taken as a direct proxy for the cyclic blade pitch response since for these rotors the lag-pitch coupling coefficient was kinematically determined to be one. As a result, Figs. 12 and 13 showing the lag response to changes in input drive voltage amplitude may be read as depicting the cyclic blade pitch obtained by this rotor system. Once again both the large and small rotors at both high and low speeds show a low amplitude knee associated with static friction, after which a linear growth in the blade pitch response begins. There is more evidence of the blades hitting the hard kinematic stops for the highest drive amplitudes in both both the small and large rotor. In high speed tests the rotors were not driven much beyond this point due to thermal limits in the small rotor and risk of shock damage to the large rotor. In these experiments both the 10 cm and 1 m diameter propeller were driven up to a cyclic pitch amplitude of approximately 10°. There is notably more variation in the experimentally obtained response phase as well as a larger discrepancy with respect to the model of up to 30°. Some of this is an expected accumulation of modeling errors as the measurements become further removed from the input signal. For example, it should not be surprising that if the hub speed response has more phase delay than expected, the lag response will as well. At the same time, it is likely that limits in the timing accuracy of the photographic measurement method or unmodeled system delays affect the phase determination in the highest speed tests, resulting in increasing apparent phase delay at high operating speed.

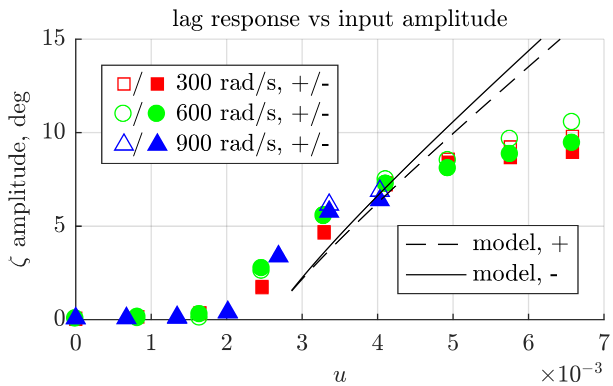

Fig. 12 Lag (pitch) angle response in small rotor.

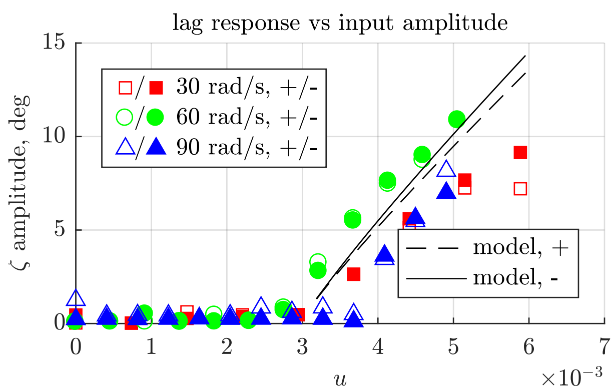

Fig. 13 Lag (pitch) angle response in large rotor.

The flapping response for the small and large rotors are depicted in Fig. 14 and 15. As in previous work [3] the response amplitude is significantly overestimated by the model, which is an expected result of neglecting to model the nonsymmetric inflow distribution obtained during constant heavy cyclic. The large rotors tests show a different unexpected result, which is that the mid-speed test at 60 rad/s consistently yields proportionality higher response amplitudes than the low speed or high speed tests. This may be due to an unmodeled structural resonance in either the large rotor or the large rotor fixture. The acetal blades are moderately flexible and have a nonrotational natural flapping frequency of 64 rad/s in cantilever from the blade grips. In general, introducing structural stiffness into the model breaks dynamic similarity across operating speeds because the flapping frequency ratio becomes speed dependent, and this may explain the result shown here. Nevertheless, the agreement between the high and low speed tests far from resonance is very good, which suggests the broad scaling trends implied the the nondimensional equations remain useful. The small rotors in MAV are typically quite stiff in comparison to full scale aircraft, and the rigid blade modeling assumptions which are satisfactory for many small scale rotors may not be appropriate at large scale.

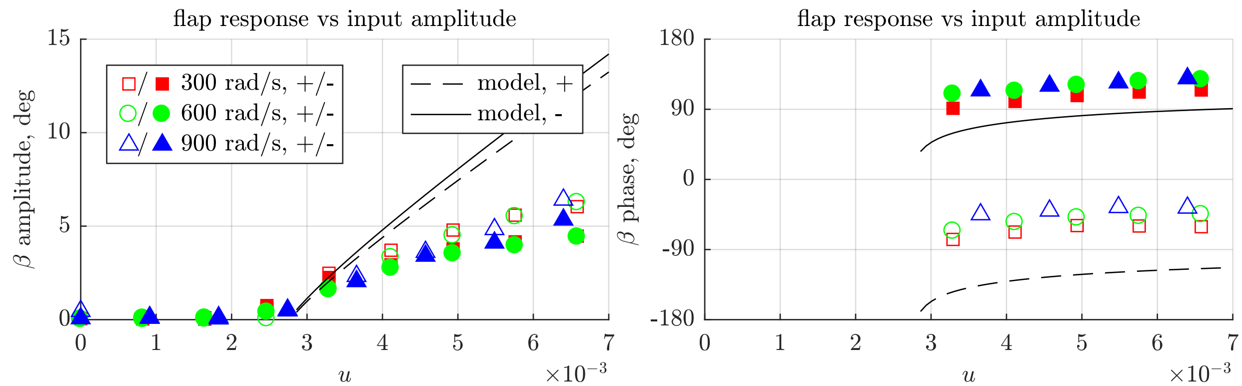

Fig. 14 Flap angle response in small rotor.

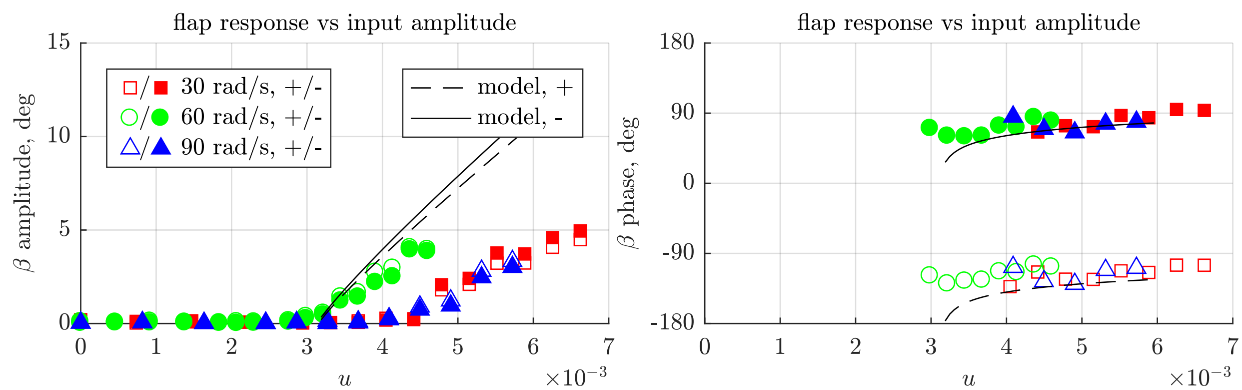

Fig. 15 Flap angle response in large rotor.

IX. Conclusion

Cyclic blade pitch control can be practiced in helicopters without the need for a swashplate system by using the passive dynamics of flexible rotors to exploit the high-bandwidth capabilities of electric drive motors. This technique has now been demonstrated in rotors as small as 10 cm and as large as 1 m, at operating speeds as slow as 300 RPM and as fast as 9000 RPM. A semi-analytic lump parameter model has predictive power over this entire operational range. We provide prescriptive guidelines for constructing dynamically similar rotors at different scales, and experimental results show that one can confidently extrapolate the dominant inertial dynamics from a small model scale rotor to a larger test rotor. For a given aircraft weight larger, slower rotors place a proportionately smaller torque modulation burden on the drive motor than smaller, faster rotors. In addition, assuming Froude scaling of aircraft systems, the dynamics are fundamentally insensitive to the gross scale of the aircraft and therefore one might find this technology to be suitable both for very small and very large aircraft. However, the power plant capacity and safety through redundancy requirements for large manned aircraft present unique challenges not found in unmanned and micro air vehicles.

Acknowledgements

This material is based upon work supported by the National Science Foundation under Grant No. 1138847.

References

[1] Paulos, J., and Yim, M., "An Underactuated Propeller for Attitude Control in Micro Air Vehicles," *2013 IEEE/RSJ International Conference on Intelligent Robots and Systems (IROS)*, Tokyo, 2013, pp. 1374–1379. doi:10.1109/IROS.2013.6696528.

[2] Paulos, J., and Yim, M., "Flight Performance of a Swashplateless Micro Air Vehicle," *2015 IEEE International Conference on Robotics and Automation (ICRA)*, Seattle, WA, 2015, pp. 5284–5289. doi:10.1109/ICRA.2015.7139936.

[3] Paulos, J., and Yim, M., "Cyclic Blade Pitch Control for Small UAV without a Swashplate," *AIAA Atmospheric Flight Mechanics Conference, SciTech Forum*, Grapevine, TX, 2017. doi:10.2514/6.2017-1186.

[4] Olson, E., "AprilTag: A Robust and Flexible Visual Fiducial System," *2011 IEEE International Conference on Robotics and Automation (ICRA)*, Shanghai, 2011, pp. 3400–3407. doi:10.1109/ICRA.2011.5979561.

[5] Hunt, G. K., "Similarity Requirements for Aeroelastic Models of Helicopter Rotors," Tech. Rep. RAE 72005 (ARC 33730), 1972.

[6] Singleton, J. D., and Yeager, W. T., "Important Scaling Parameters for Testing Model-Scale Helicopter Rotors," *Journal of Aircraft*, Vol. 37, No. 3, 2000, pp. 396–402. doi:10.2514/2.2639.

[7] Wolowicz, C. H., Brown, J. S., and Gilbert, W. P., "Similitude Requirements and Scaling Relationships as Applied to Model Testing," Tech. Rep. NASA-TP-1435, Aug. 1979.

[8] Mettler, B., Dever, C., and Feron, E., "Scaling Effects and Dynamic Characteristics of Miniature Rotorcraft," *Journal of Guidance, Control, and Dynamics*, Vol. 27, No. 3, 2004, pp. 466–478. doi:10.2514/1.10336.

[9] Kushleyev, A., Mellinger, D., Powers, C., and Kumar, V., "Towards a Swarm of Agile Micro Quadrotors," *Autonomous Robots*, Vol. 35, No. 4, 2013, pp. 287–300. doi:10.1007/s10514-013-9349-9.

[10] Alvarenga, J., Vitzilaios, N. I., Rutherford, M. J., and Valavanis, K. P., "Scaled Control Performance Benchmarks and Maneuvers for Small-Scale Unmanned Helicopters," *2015 IEEE 54th Conference on Decision and Control (CDC)*, 2015, pp. 6035–6042. doi:10.1109/CDC.2015.7403168.

[11] Lorenz, R. D., "Flight Power Scaling of Airplanes, Airships, and Helicopters: Application to Planetary Exploration," *Journal of Aircraft*, Vol. 38, No. 2, 2001, pp. 208–214. doi:10.2514/2.2769.

[12] Karydis, K., and Kumar, V., "Energetics in Robotic Flight at Small Scales," *Interface Focus*, Vol. 7, No. 1, 2017. doi:10.1098/rsfs.2016.0088.

[13] Leishman, G. J., *Principles of Helicopter Aerodynamics*, 2nd ed., Cambridge University Press, Cambridge, 2006.

[14] Ballin, M. G., "A High Fidelity Real-Time Simulation of a Small Turboshaft Engine," Tech. Rep. NASA-TM-100991, Jul. 1988.

[15] Duyar, A., Gu, Z., and Litt, J. S., "A Simplified Dynamic Model of the T700 Turboshaft Engine," *American Helicopter Society Annual Forum*, Washington, D.C., 1992.